Research Square

Preprints are preliminary reports that have not undergone peer review.
They should not be considered conclusive, used to inform clinical practice,
or referenced by the media as validated information.

# Frequency-dispersive magnetic anisotropy dissolves the Snoek trade-off

**Jianguo Guan**

guanjg@whut.edu.cn

Wuhan University of Technology https://orcid.org/0000-0002-2223-4524

**Yifan Xu**

Wuhan University of Technology

**Ning Xu**

Wuhan University of Technology

**Zhihong Chen**

Wuhan University of Technology

**Yunhao Luo**

Wuhan University of Technology

**Renjunyi Zhao**

Wuhan University of Technology

**Yuchen Hu**

Wuhan University of Technology

**Chenxi Liao**

Wuhan University of Technology

**Shuiqing Lu**

Wuhan University of Technology

**Miaomiao Bi**

Wuhan University of Technology

**Yajiao Ke**

School of Physics and Mechanics, Wuhan University of Technology

**Yanli Li**

Wuhan University of Technology

**Wei Li**

Wuhan University of Technology

**Physical Sciences - Article**

**Keywords:**

**Posted Date:** November 27th, 2026

**DOI:** https://doi.org/10.21203/rs.3.rs-11868226/v1

**License:** This work is licensed under a Creative Commons Attribution 4.0 International License.
Read Full License

**Additional Declarations:** There is **NO** Competing Interest.

**Frequency-Dispersive Magnetic Anisotropy Dissolves the Snoek Trade-off**

Yifan Xu (徐逸凡) [1], Ning Xu (徐宁) [2], Zhihong Chen (陈志宏) [3,4 †], Yunhao Luo (罗运嵩) [3], Renjunyi Zhao (赵任俊毅) [3], Yuchen Hu (胡雨晨) [3], Chenxi Liao (廖晨曦) [1], Shuiqing Lu (陆水清) [3], Miaomiao Bi (毕淼淼) [3], Yajiao Ke (柯亚娇) [3], Yanli Li (李艳丽) [3], Wei Li (李维) [1,4], Jianguo Guan (官建国) [1,4 †]

---

[1] State Key Laboratory of Advanced Technology for Materials Synthesis and Processing, Wuhan University of Technology, Wuhan 430070, China.

[2] School of Information Engineering, Wuhan University of Technology, Wuhan 430070, China.

[3] School of Physics and Mechanics, Wuhan University of Technology, Wuhan 430070, China.

[4] Wuhan CyneMag Technology Co., Ltd, Wuhan 430083, China.

[†] Zhihong Chen (z_chen@whut.edu.cn), Jianguo Guan (guanjg@whut.edu.cn).

**High magnetic permeability enables compact and efficient electromagnetic devices, but the Snoek trade-off associates high permeability with low resonance frequency. Interphase exchange coupling is conventionally assumed to be constant and frequency-independent. Here we show that exchange coupling among magnetic regions with distinct local anisotropies can make the effective anisotropy field frequency-dependent. As a proof of concept, Mn addition to FeSiAl produces two coherent $D0_3$ phases with perpendicular easy axes. At low frequency their moments rotate together and partially compensate the local anisotropy; at high frequency their rotations become less collective and intrinsic anisotropies dominate the precession. The element-substituted alloys significantly improve the initial permeability while showing a retained or increased apparent resonance frequency compared with the FeSiAl. Ferromagnetic-resonance measurements and joint fits of the complex permeability support a dispersive effective anisotropy rather than a frequency-independent constant. A composite absorber of FeMnSiAl dispersed in silicone resin shows microwave absorption exceeding 90% over 0.96–1.98 GHz at a thickness of 2.7 mm, only 8.2% of the band-limited Rozanov-equivalent thickness of a nonmagnetic absorber. This design of coherence among moment precessions establishes a degree of freedom for extending strong magnetic response to higher frequencies without the usual permeability-resonance penalty.**

Modern electronic systems are moving toward miniaturization and integration, requiring more functions to fit into less space [1-3]. A high initial magnetic permeability ($\mu_i$) is critical because it provides sufficient magnetic response within constrained volume. In conventional soft magnets, which possess a given saturation magnetization ($M_s$) and usually exhibit a constant anisotropy, however, the Snoek limit indicates that enhancing $\mu_i$ inevitably compromises the high-frequency response in the MHz-GHz regimes [4]. These challenges have persisted for decades in high-frequency applications across the communications, semiconductor, and energy sectors [5].

The Snoek trade-off can be understood through a constant effective anisotropy field ($H_k$). A smaller $H_k$ makes moments easier to rotate during magnetization and raises $\mu_i$ [6], but it also weakens the restoring force, slows the moment precession, and lowers the resonance frequency ($f_r$). Quantitatively, for a bulk magnet with constant $H_k$ , the product of $f_r$ and $\mu_i - 1$ is proportional to $M_s$ [4, 7]. Introducing shape anisotropy relaxes this limit in a flattened magnet by making the restoring fields unequal along two directions [8]: A weak in-plane restoring field governs the static response, whereas a stronger out-of-plane restoring field dominates the resonance. Although further increasing the degree of flattening yields diminishing improvements in magnetic permeability, this approach shows that the Snoek trade-off can be relaxed by differentiating $H_k$ between the static and dynamic magnetization processes [9-11].

Exchange coupling among fine grains or phases has long been regarded as an effective route to enhance $\mu_i$ or $f_r$. In all these approaches, however, the moments of different regions are usually assumed to remain equally coherent in static and dynamic responses [12-16], difficult to achieve the simultaneous enhancement of both $\mu_i$ and $f_r$. Here we propose that exchange coupling between regions with different local anisotropies can generate a frequency-dependent effective $H_k$. Under a

slowly varying field, exchange keeps the moments nearly collinear, so their anisotropies can compensate each other and $\mu_i$ is enhanced. If the coupling is strong but not completely rigid, faster excitation allows a phase difference to develop between their precessions [17, 18]; the local anisotropies then contribute more strongly and the effective $H_k$ rises. This behavior may occur among grains, phases or magnetic layers.

As a proof of concept, Mn addition was used to form two coherent $D0_3$ phases within FeSiAl. Two identifiable phases with perpendicular easy axes provide a clear test of the idea, and the characteristic size of the second $D0_3$-(Fe,Mn)SiAl phase lies in the range that permits interphase exchange coupling while still allowing relative moment motion. Compared with the FeSiAl reference, the resultant FeMnSiAl powders nearly double $\mu_i$ while preserving an apparent $f_r$ near 0.8 GHz. The product of $\mu_i - 1$ and $f_r$ increases from approximately 3.4 to 7.2 GHz, far exceeding the modest $M_s$ variation. Ferromagnetic resonance behavior and permeability fitting further support a frequency-dispersive $H_k$. The FeMnSiAl-based coating enables >90% absorption across 0.96–1.98 GHz at only 2.7 mm. This work establishes the frequency-dependent coherence of coupled magnetic regions as a designable degree of freedom to decouple the Snoek trade-off between $\mu_i$ and high-frequency performance.

## Constructing coherent dual $D0_3$ phases

A dispersive $H_k$ is expected to arise from competition between exchange stiffness and distinct local anisotropies (**Fig. 1a**). Realizing it requires local easy directions that compete, an interface that transmits exchange, and a phase size that permits coupling without locking both phases into a rigid unit. FeSiAl supplies a soft-magnetic $D0_3$ host in which Mn can modify the local magnetic environment. First-principles calculations predict preferred magnetization along [001] and [100] for $D0_3$-FeSiAl, but along [010] for the Mn-substituted $D0_3$ model (**Fig. 1b**). This orthogonal contrast provides sufficiently compensating anisotropy torques during collective rotation.

All synthesized powders ($Fe_{85-x}Mn_xSi_{9.6}Al_{5.4}$, denoted $FM_xSA$) were prepared using an identical route. Their comparable morphology, grain sizes and residual strains reduce the likelihood that processing differences account for the permeability variation (**Figs. S1-S5**). In the Mn-containing alloy, an elemental line scan reveals Mn-rich regions within individual grains (**Fig. 1c**). TEM images show nanoscale regions separated from the matrix by closely matched crystal planes (**Fig. 1d**). The measured lattice mismatch is about 1.77%. Peak splitting in the XRD pattern is consistent with two $D0_3$-type lattices of slightly different dimensions (**Fig. 1d,e**). Mn K-edge EXAFS, local composition, Mössbauer spectra and first-principles calculations support substitution of Mn for body-centered Fe in the $D0_3$ supercell (**Fig. 1c,f**, **Tables S1-S4**). Together, these observations identify a $D0_3$-FeSiAl matrix and coherent $D0_3$-(Fe,Mn)SiAl regions, with relative fractions of approximately 64.6 wt.% and 35.4 wt.%, respectively.

The Mn-rich regions are typically about 10–30 nm across. Their sizes overlap the estimated 9–31 nm range in which exchange can link the phases while still allowing relative magnetic motion [19] (**Supplementary Discussion 4**). $FM_{3.2}SA$ therefore provides a direct test of our design. The initial

permeability $\mu_i$ of $FM_{3.2}SA$ in wax reaches 9.96, nearly twice the 5.30 of the FeSiAl reference (denoted as FSA), yet both imaginary permeability spectra show a loss peak around 0.8 GHz (**Fig. 1g**). Together, these measurements pose the mechanistic question: what makes low-field rotation easier while leaving the loss-peak frequency essentially unchanged?

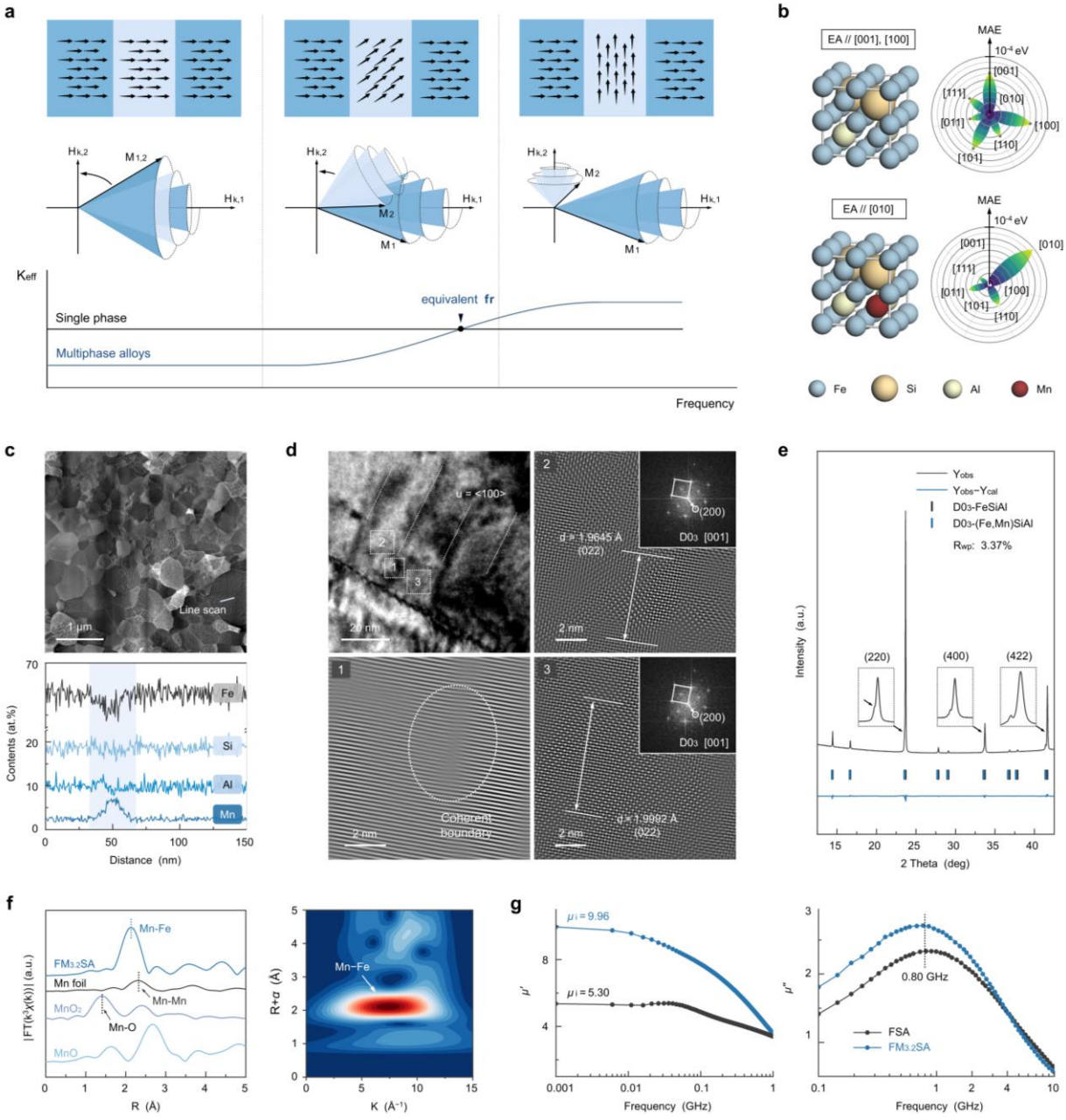


**Fig. 1 | Design and realization of coherent dual-$D0_3$ phases for frequency-dispersive magnetic anisotropy. a** Design schematic of frequency-dispersive magnetic anisotropy in alloys with

multiple coupled phases, arising from competition between exchange coupling and distinct local anisotropies. **b** $D0_3$-based atomic models and calculated magnetocrystalline anisotropy energies for FeSiAl and Mn-substituted FeSiAl. **c** STEM image and corresponding EDS line scan of synthesized $FM_{3.2}SA$. **d** Bright-field and HR-TEM images showing distinct $D0_3$-type supercells and their interfaces. **e** Rietveld refinement of synchrotron XRD pattern of $FM_{3.2}SA$. **f** EXAFS spectra and Mn K-edge fitting results for $FM_{3.2}SA$ and reference samples. **g** Doubled $\mu_i$ and preserved $f_r$ in $FM_{3.2}SA$ compared with the FSA reference.

**Frequency-dependent mode differentiation**

At low frequencies, exchange coupling constrains the moments of the two coherent $D0_3$ phases to rotate nearly collinearly, despite their distinct local easy axes. For two perpendicular easy directions, one phase partly counters the restoring torque of the other. The collective anisotropy can therefore be smaller than either local contribution, increasing rotational permeability (**Supplementary Discussion 4**). The contrast of local anisotropy is illustrated by magnetic force microscopy (MFM) images of an unusually large $D0_3$-(Fe,Mn)SiAl region (~179 nm). This dimension exceeds the characteristic exchange length and allows distinct local magnetic contrast to be resolved (**Fig. 2a**). However, most Mn-rich regions are substantially smaller and remain exchange constrained by the surrounding matrix. The Lorentz TEM reveals that the magnetic domains extend over a number of nanoscale second-phase regions (**Fig. 2b**). Atomically smooth coherent interfaces preserve the continuity of the bcc-Fe sublattice across the phase boundary, sustaining short-range direct exchange interaction between Fe moments on either side [20]. Additionally, negligible domain-wall displacement under weak applied magnetic fields indicates

that the dominant low-field response comes from the collective moment rotation instead.

Such collective behavior, however, no longer remains rigid under excitation at increasing frequency. As the distinct local anisotropy torques become increasingly important instead of exchange coupling, a gradual evolution occurs from exchange-constrained collective motion toward isolated precessions.

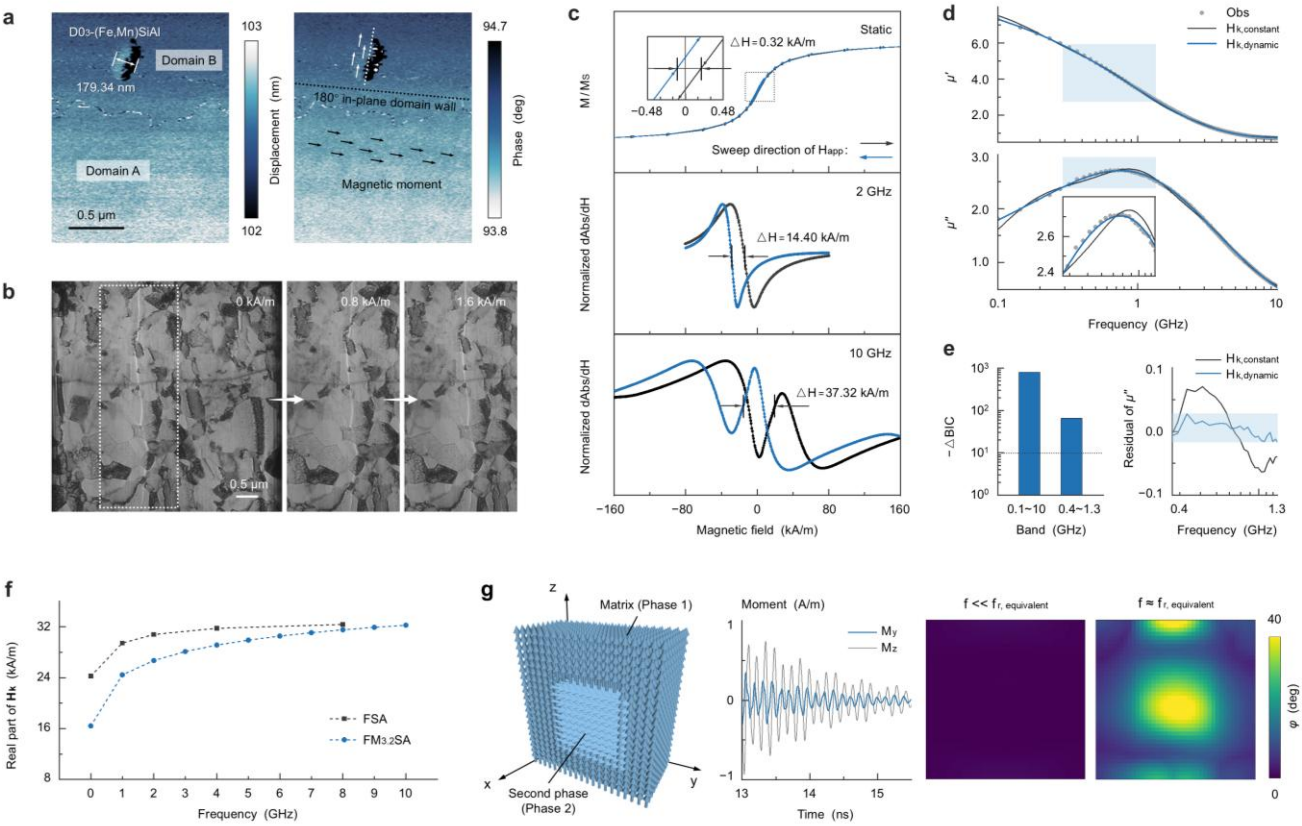


**Fig. 2 | Static anisotropy compensation and frequency-dependent magnetic dynamics. a** MFM images of $FM_{3.2}SA$, highlighting an unusually large $D0_3$-(Fe,Mn)SiAl region and the corresponding local magnetic contrast. **b** Lorentz TEM images of $FM_{3.2}SA$ under applied magnetic fields of 0, 0.8, and 1.6 kA/m, showing micro-scale magnetic domains with limited domain-wall displacement. **c** Static hysteresis loop of $FM_{3.2}SA$ and its field-swept FMR spectra measured under opposite field-sweep directions at 2 and 10 GHz. **d** Fits of the dispersive permeability spectra for $FM_{3.2}SA$

composites using constant- and dynamic-$H_k$ models, with an enlarged view provided for the frequency range of 0.4 to 1.3 GHz, and **e** comparison of the fitting quality between the two models (ΔBIC is defined as the BIC of the dynamic-$H_k$ model minus that of the constant-$H_k$ model). **f** Frequency dispersion of the real part of $H_k$ supported by dispersive permeability and FMR spectra. **g** Two-phase micromagnetic model (80×80×20 nm), with decomposed magnetic-moment components and simulated maps of interphase precession-phase difference below and near resonance.

Field-swept ferromagnetic resonance (FMR) provides experimental evidence for this evolution. Despite a static hysteresis displacement of only 0.32 kA/m, $FM_{3.2}SA$ exhibits pronounced sweep-direction-dependent shifts of the FMR response, reaching 14.40 kA/m at 2 GHz and 37.32 kA/m at 10 GHz (**Fig. 2c**). By contrast, FSA shows a similarly small static hysteresis but much weaker FMR shifts of 2.94–3.34 kA/m over 2–8 GHz (**Figs. S14** and **S15**). This striking contrast reveals a substantially stronger frequency-dependent sensitivity of $FM_{3.2}SA$. Moreover, its FMR spectra evolve from a predominantly single observable mode at 1–6 GHz to two resolvable components at 7–10 GHz (**Fig. 2c**, **Figs. S12** and **S13**). Consequently, the magnetization dynamics of the moments in the dual-phase $FM_{3.2}SA$ can be summarized in three regimes: i) collinear collective precession at static or low frequencies, ii) dephased collective precession around resonance (0.1–6 GHz), and iii) differentiated precessions at high frequencies (8–10 GHz).

Such mode differentiation is dominated by the competition between local anisotropies and interphase exchange coupling [18]. As the frequency increases, the magnetic moments of each phase tend to precess along their respective easy axes, which weakens the anisotropy compensation and gives rise to a frequency-dispersive $H_k$. A dynamic $H_k$ provides a new perspective on why the

magnetic performance of $FM_{3.2}SA$ violates the Snoek limit. Accordingly, joint fits of its complex permeability spectra were conducted. Although constant- and dynamic-$H_k$ descriptions reproduce the overall spectral trends well, the latter provides a significantly better representation of the resonance region (**Fig. 2d**). Specifically, within 0.4–1.3 GHz, the fitting quality ($R^2$) for $\mu''$ improves from 0.06789 to 0.95545, while the Bayesian information criterion (BIC) decreases by 65.93 despite the penalty for the additional parameter (**Fig. 2e**, **Table S7**). Over the full 0.1–10 GHz, the BIC improvement also reaches 789.46. The extracted effective stiffness increases with frequency (**Fig. 2f**). This is consistent with the progressive reduction of rigid interphase coherence inferred from FMR and micromagnetic simulations (**Fig. 2g**).

Collectively, these independent observations support a frequency-dispersive effective $H_k$. Strong anisotropy compensation promotes moment rotation at low frequencies, whereas the increasing participation of relative magnetic motion progressively restores effective stiffness as frequency increases. The conventional Snoek trade-off between permeability and resonance is thus relaxed.

**Design rules for anisotropy compensation**

The frequency-dependent effective $H_k$ established above provides a design strategy for tailoring $\mu_i$ and resonance behavior. In the low-field exchange-constrained limit, two magnetic phases (A and B) with distinct easy axes exhibit an effective anisotropy [21]

$$K_{eff} = \sqrt{(VK_A)^2 + [(1-V)K_B]^2 + 2V(1-V)K_A K_B \cos(2\triangle\alpha)} \quad ,$$

where $V$ is the volume fraction of phase A, $K_A$ and $K_B$ are the intrinsic uniaxial magnetocrystalline anisotropy constants, and $\triangle\alpha$ is the angular difference between their easy-axis directions in the

rotation plane (**Supplementary Discussion 4**). Notably, the effective anisotropy depends not only on the relative phase fractions, but also on the intrinsic anisotropy magnitudes and, critically, the angular relationship between their easy axes. For instance, parallel easy axes reinforce the anisotropy contributions, whereas perpendicular orientations allow partial compensation.

The resonance response is governed by the effective dynamic restoring stiffness. In the small-angle approximation of moment precession, the apparent resonance frequency [22, 23]

$$f_r = \frac{\gamma \mu_0}{2\pi} \sqrt{H_1(f_r)\ H_2(f_r)}$$

where $H_1(f_r)$ and $H_2(f_r)$ denote the two orthogonal transverse restoring fields, incorporating magnetocrystalline anisotropy, demagnetization and exchange coupling (**Supplementary Discussion 6**). Accordingly, strong low-frequency anisotropy compensation and sufficient high-frequency restoring stiffness can be simultaneously achieved, thus allowing $\mu_i$ and $f_r$ to be tailored beyond the conventional single-anisotropy constraint.

We first examined this principle by varying the Mn content in FeMnSiAl alloy powders (**Fig. 3a,b**). Mn doping modifies the relative contributions of the two coherent $D0_3$ phases, thereby changing their collective anisotropy compensation. The measured anisotropy proxy, $M_s^2/\mu_i$ [24], follows the calculated compensation trend. Notably, $FM_{3.2}SA$ exhibits nearly twice the initial permeability of FSA without a proportional downward shift of $f_r$. This behavior is consistent with the strongly reduced static stiffness and its partial recovery in the GHz regime, as supported by the FMR, dynamic-$H_k$ fitting and micromagnetic simulations (**Fig. 2**).

We next explored the influence of intrinsic anisotropy through Cr, Co and Ni substitution. First-principles calculations reveal distinct magnetocrystalline anisotropy magnitudes and angular dependences among the substituted structures (**Fig. 3c,f**). Compared with FSA, all $FX_{3.2}SA$ (X = Cr,

Co, and Ni) alloy powders exhibit a reduction in static $H_k$ and increases in both $\mu_i$ and magnetic-loss peak frequencies (**Fig. 3d,e,g**), illustrating an experimentally accessible direction for improving the Snoek limit. Notably, the Co- and Cr-substituted structures exhibit a larger calculated anisotropy constant ($K_1$) than the Ni-substituted, yet the Ni-containing alloy shows the highest magnetic-loss peak frequency. This non-monotonic relationship indicates that the resonance response cannot be determined by $K_1$ alone, but also depends on the effective transverse stiffness of the coupled system.

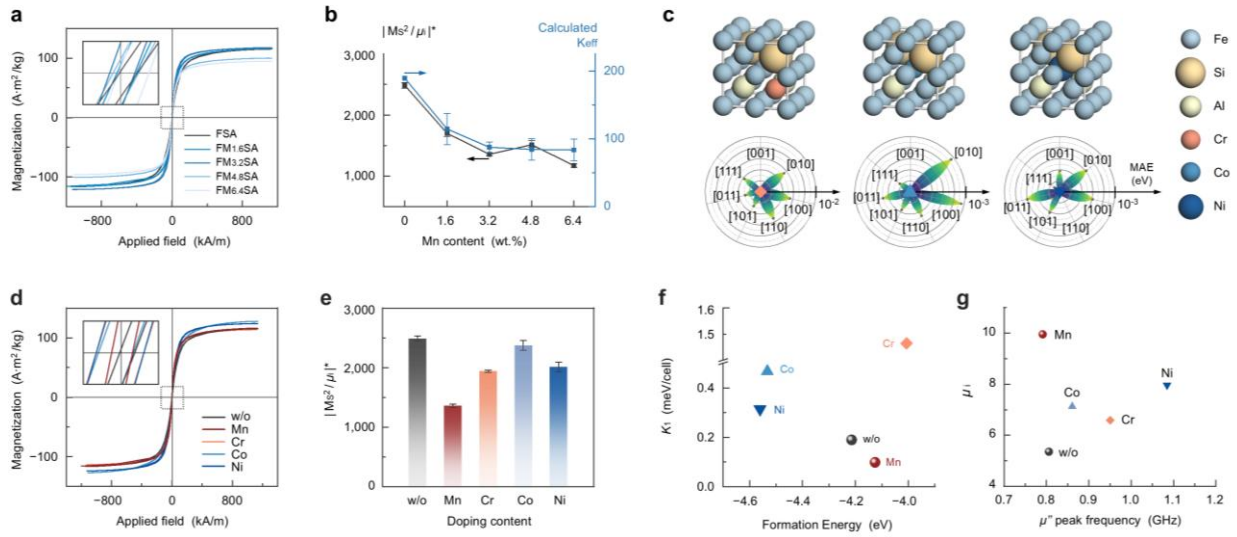


**Fig. 3 | Composition-based validation of anisotropy compensation and dynamic-coherence design. a** Hysteresis loops for the Mn-content series. **b** Measured magnetization-derived anisotropy proxies and their static compensation estimates versus Mn content. For $|M_s^2/\mu_i|$*, symbols represent the mean value (n = 5), with error bars denoting the range; for calculated $K_{eff}$, error bars reflect the uncertainties in XRD-derived phase fractions. **c** Atomic models and calculated magnetic anisotropy energies of Cr-, Co-, and Ni-substituted $D0_3$ supercells. **d** Hysteresis loops, **e** measured magnetization-derived anisotropy proxies, **f** calculated formation energies, magnetocrystalline anisotropy constants, and **g** comparison of static $\mu_i$ and $\mu''$-peak positions among the undoped and

transition-metal-doped FeSiAl-based alloy powders.

Importantly, this design concept may extend beyond multi-phase alloys. The nominally single-phase FSA reference also exhibits a moderate frequency dependence of its effective $H_k$, increasing from static 24.12 kA/m to 32.33 kA/m at 10 GHz (**Fig. S14, Table S6**). Its complex magnetic permeability spectra cannot be reproduced by the constant-$H_k$ model either (**Fig. S19**, **Table S7**). These observations are consistent with a possible contribution from exchange-coupled grains with different local anisotropy orientations. More generally, similar effects may arise from intergrain coupling in nanocrystalline magnets, interphase coupling in core-shell structures [25], or interlayer coupling in magnetic multilayers [26, 27]. Beyond regulation of intrinsic magnetocrystalline anisotropy, engineering the dynamic coherence through magnitude and relative orientations offers an additional degree of freedom for tailoring the permeability-resonance trade-off.

**An extremely thin microwave absorber**

Higher permeability is significant for microwave absorbers, while excessive electrical conduction and permittivity increase front-surface reflection. The coherent dual-$D0_3$ phases in FeMnSiAl alloys enhance $\mu_i$ while reducing electrical conductivity and permittivity. Compared to FSA, the absorber with $FM_{3.2}SA$ has lower real permittivity, a shifted dielectric-loss spectrum and an additional relaxation feature (**Fig. 4a,b**). At similar powder compaction densities, its measured DC conductivity is nearly two orders of magnitude lower (**Fig. 4c**, **Fig. S21**). The numerous internal boundaries hinder long-range carrier transport, leading to charge accumulation near interfaces and consequent variations in the local electrostatic response and the extra relaxation [28, 29] (**Fig. S22**).

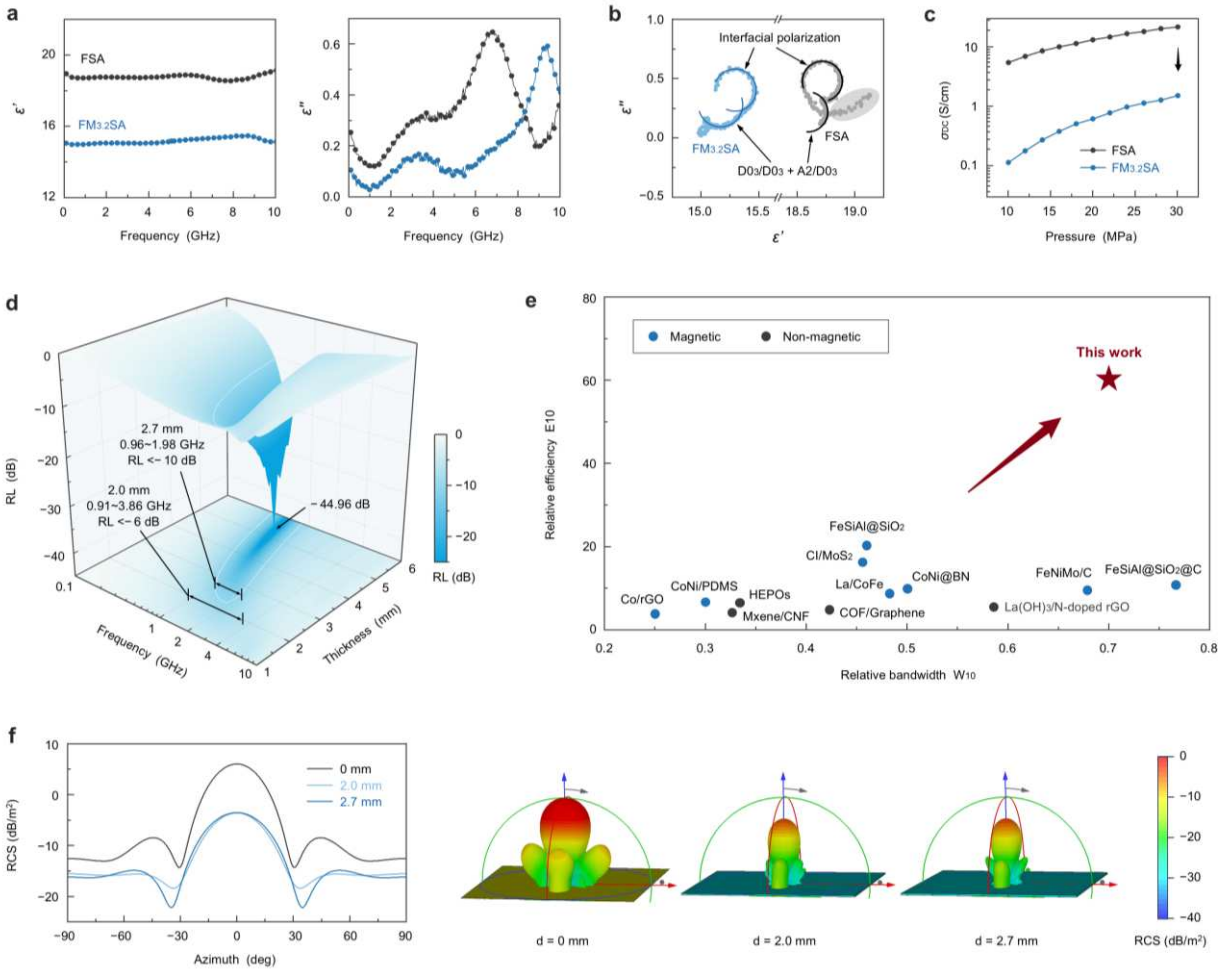


**Fig. 4 | Dielectric response and microwave-absorption performance in 0.3–10 GHz. a** Real permittivity $\varepsilon'$ and imaginary permittivity $\varepsilon''$ of the FSA and $FM_{3.2}SA$ wax composites, and **b** Cole-Cole representations of their complex permittivity. **c** DC conductivity of the FSA and $FM_{3.2}SA$ alloy powders. **d** Calculated reflection loss (*RL*) of $FM_{3.2}SA$/SR composites. **e** Microwave absorption performance compared with previously reported absorbers [30-41]. **f** Simulated far-field radar cross section (RCS) for $FM_{3.2}SA$/SR composite coated plates at 2 GHz.

We incorporated $FM_{3.2}SA$ powders into silicone resin (SR) and calculated the reflection loss (*RL*) from the measured electromagnetic parameters (**Fig. 4d**, **Figs. S24** and **S25**). At 2.7 mm, the *RL* reaches −12.37 dB at 1.35 GHz, and absorption exceeds 90% over 0.96–1.98 GHz, nearly the

whole L-band (**Fig. 4d**). Another 2.0-mm case also exceeds 75% absorption over 0.91– 3.86 GHz. Even when the thickness is reduced to only 1.9 mm, the coating maintains >75% absorption over 1.04–4.00 GHz. These results show that the preserved magnetic response in 0.3–4 GHz can be effectively turned into microwave absorption in the corresponding band at a thin thickness.

The thickness advantage becomes clearer when compared with a nonmagnetic reference over the same measured 0.3–4 GHz window. For the 2.7-mm case, the band-limited Rozanov-equivalent nonmagnetic thickness is 32.94 mm, giving a thickness-compression factor $C_{mag}$ = 8.20% [42] (**Table S8**). The bandwidth and thickness also compare favorably with reported low-frequency absorbers (**Fig. 4e**). Finally, far-field RCS simulations show smaller principal scattering lobes for $FM_{3.2}SA$ coating than for the bare metal plate (**Fig. 4f**, **Fig. S26**). The structural design thus benefits the coating in two ways: it sustains magnetic response in the targeted band and moderates the electrical response needed for the incident wave to penetrate.

It is worth noting that the storage sensitivity of intermediate powders necessitates careful control of processing intervals, and scalable manufacturing protocols remain to be explored (**Fig. S27**). Even so, the fully processed $FM_xSA$ alloy powders remain phase-stable and exhibit environmental tolerance comparable to that of FSA (**Figs. S28-S31**).

## Conclusions

In this work, we demonstrate that frequency-dependent magnetic coherence provides an additional degree of freedom for relaxing the Snoek trade-off in soft-magnets. By constructing two nanoscale coherent $D0_3$ phases with perpendicular easy axes, the FeMnSiAl alloy enables exchange-constrained collective rotation and anisotropy compensation at low frequencies,

increasing the $\mu_i$ from 5.30 to 9.96 without a proportional reduction in the $f_r$ (~0.8 GHz). Crucially, the internal magnetic response does not remain rigidly coherent as frequency increases. Field-swept FMR reveals strongly enhanced magnetic-history dependence and progressive mode differentiation, while micromagnetic simulations capture the increasing interphase precessional phase difference. Consistently, a frequency-dependent effective field, $H_k$, provides a substantially improved description of the complex permeability, particularly around resonance. To conclude, these findings establish a physical picture in which static anisotropy compensation enhances low-frequency permeability, whereas the dynamic restoring stiffness is partially recovered at high frequencies, thereby relaxing the Snoek trade-off. As a result, the FeMnSiAl-based absorber achieves absorption above 90% over 0.96–1.98 GHz at a thickness of 2.7 mm.

Beyond the specific $FM_{3.2}SA$ alloy, the results suggest a broader strategy for engineering magnetic coherence by tailoring the magnitudes, orientations and relative contributions of local anisotropies. The Mn-composition series and substitutional alloys illustrate the tunability of the anisotropy. The observed weak frequency-dispersion of $H_k$ in FSA suggests that the same principle may extend to exchange-coupled nanocrystalline magnets and magnetic multilayers. For practical applications, phase stability and precise control over second-phase dimensions remain key challenges. To enable the inverse design of soft magnets with targeted permeability and resonance characteristics, whether this dynamic-coherence engineering extends to other crystal symmetries remains to be explored. Generally, the dispersive $H_k$ should be read as an effective response parameter. Engineering the frequency evolution of internal magnetic coherence offers an additional and largely unexplored route to tailoring permeability and resonance.

## References


1. He, M. et al. Low-frequency microwave absorption composites, *Advanced Science* **12**, e11580 (2025).
2. Li, H. et al. High-frequency FeSiAl-based soft magnetic composites via simultaneously suppressed eddy and hysteresis losses, *Nature Communications* **16**, 9563 (2025).
3. Qi, Z. et al. A wearable repetitive transcranial magnetic stimulation device, *Nature Communications* **16**, 2731 (2025).
4. Snoek, J. L. Dispersion and absorption in magnetic ferrites at frequencies above one Mc/s, *Physica* **14**, 207-217 (1948).
5. Guo, R. et al. Advances and mechanistic insights into low-frequency (sub-8 GHz) microwave-absorbing materials: A critical review bridging conventional architectures and emerging frontiers, *Advances in Colloid and Interface Science* **344**, 103612 (2025).
6. Han, L. et al. A mechanically strong and ductile soft magnet with extremely low coercivity, *Nature* **608**, 310-316 (2022).
7. Bai, G. et al. Vortex-based soft magnetic composite with ultrastable permeability up to gigahertz frequencies, *Nature Communications* **15**, 2238 (2024).
8. Acher, O. & Dubourg, S. Generalization of Snoek's law to ferromagnetic films and composites, *Physical Review B* **77**, 104440 (2008).
9. Walser, R. K., Win, W. & Valanju, P. M. Shape-optimized ferromagnetic particles with maximum theoretical microwave susceptibility, *IEEE Transactions on Magnetics* **34**, 1390-1392 (1998).
10. Xu, H. et al. High-frequency soft magnetic properties in $Th_2Ni_{17}$-type $Gd_2Co_{17}$ films enabled

by intrinsic planar anisotropy, *Acta Materialia* **302**, 121678 (2026).

11. Zhao, R. et al. Highly anisotropic $Fe_3C$ microflakes constructed by solid-state phase transformation for efficient microwave absorption, *Nature Communications* **15**, 1497 (2024).

12. Liu, J. et al. Scalar permeability microstructure model considering crystallographic texture and grain size for magnetic evaluation of anisotropy in steel, *Acta Materialia* **289**, 120863 (2025).

13. Zhou, J. et al. Ultrahigh permeability at high frequencies via a magnetic-heterogeneous nanocrystallization mechanism in an iron-based amorphous alloy, *Advanced Materials* **35**, 2304490 (2023).

14. Herzer, G. Grain structure and magnetism of nanocrystalline ferromagnets, *IEEE Transactions on Magnetics* **25**, 3327-3329 (1989).

15. Herzer, G. Grain size dependence of coercivity and permeability in nanocrystalline ferromagnets, *IEEE Transactions on Magnetics* **26**, 1397-1402 (1990).

16. Mingyue, Y. et al. Magnetic composite formed by exsolution forenhanced exchange coupling and breaking the permeability-frequency limitation, *Advanced Materials* **38**, e74241 (2026).

17. Liu, C. et al. Correlated spin-wave generation and domain-wall oscillation in a topologically textured magnetic film, *Nature Materials* **24**, 406-413 (2025).

18. Makiuchi, T. et al. Persistent magnetic coherence in magnets, *Nature Materials* **23**, 627-632 (2024).

19. Suzuki, K. & Cadogan, J. M. Random magnetocrystalline anisotropy in two-phase

nanocrystalline systems, *Physical Review B* **58**, 2730-2739 (1998).

20. Fullerton, E. E. et al. Exchange-spring behavior in epitaxial hard/soft magnetic bilayers, *Physical Review B* **58**, 12193-12200 (1998).

21. Stoner, E. C. & Wohlfarth, E. P. A mechanism of magnetic hysteresis in heterogeneous alloys, *IEEE Transactions on Magnetics* **27**, 3475-3518 (1991).

22. Waring, H. J. et al. Magnetization dynamics in synthetic ferromagnetic thin films, *Physical Review B* **104**, 014419 (2021).

23. Polder, D. On the theory of ferromagnetic resonance, *Physica* **15**, 253-255 (1949).

24. Herzer, G. Nanocrystalline soft magnetic materials, *Journal of Magnetism and Magnetic Materials* **157/158**, 133-136 (1996).

25. Chen, G. et al. Visualizing nanoscale interlayer magnetic interactions and unconventional low-frequency behaviors in ferromagnetic multishelled structures, *Advanced Materials* **36**, 2313411 (2024).

26. Du, H. et al. $[(FeCoB/Ru/FeCoB)/ZnO]_n$ superlattice multilayer: A real optical mode ferromagnetic resonance thick-film, *Applied Physics Letters* **116**, 152403 (2020).

27. Wang, C. et al. Dynamic interlayer exchange coupling in magnetic anisotropic FeCoB/Ru/FeCoB sandwich trilayers, *Journal of Magnetism and Magnetic Materials* **527**, 167801 (2021).

28. Zhou, X. et al. Insulating electromagnetic-shielding silicone compound enables direct potting electronics, *Science* **385**, 1205-1210 (2024).

29. Zhang, Y. et al. Simultaneous enhancement of low-frequency microwave absorption and corrosion resistance in FeSi alloys via magnetic-structural heterojunction engineering,

*Advanced Functional Materials* **35**, 2508832 (2025).

30. Shao, G. et al. Covalent organic framework-amplified polarization loss in ultralight Schottky heterojunction aerogels for low-frequency electromagnetic wave absorption, *Advanced Functional Materials* **36**, e16078 (2025).

31. Li, J. et al. Achieving ultra-low frequency microwave absorbing properties based on anti-corrosive silica-pinned flake FeSiAl hybrid with full L band absorption, *Journal of Alloys and Compounds* **888**, 161574 (2021).

32. Yao, Z. et al. Engineering flaky carbonyl iron/$MoS_2$ composites with tuned and broadband absorption towards low-frequency electromagnetic waves, *Journal of Materials Chemistry C* **12**, 16560-16573 (2024).

33. He, M. et al. Excellent low-frequency microwave absorption and high thermal conductivity in polydimethylsiloxane composites endowed by hydrangea-like CoNi@BN heterostructure fillers, *Advanced Materials* **36**, 2410186 (2024).

34. Shan, B., Wang, Y., Ji, X. & Huang, Y. Enhancing low-frequency microwave absorption through structural polarization modulation of MXenes, *Nano-Micro Letters* **16**, 212 (2024).

35. Yao, K. et al. High-entropy perovskite oxides: Morphotropic phase boundary interfacial engineering for next-generation communications, *Science Advances* **11**, eaea0362 (2025).

36. Zhang, Y. et al. Nd-, La-induced precipitate/defect in cobalt-iron magnetic alloy for strong and broadband microwave absorption, *Acta Materialia* **275**, 120042 (2024).

37. He, M. et al. Shape anisotropic chain-like CoNi/polydimethylsiloxane composite films with excellent low-frequency microwave absorption and high thermal conductivity, *Advanced Functional Materials* **35**, 2316691 (2024).

38. Qu, Y. et al. Ultrafine well-dispersed Co nanocrystals onto crumpled sphere-like rGO for superior low-frequency microwave absorption, *Carbon* **213**, 118280 (2023).
39. Yan, L. et al. Utilizing distinctive crystalline/amorphous nano-domains to facilitate multi-polarization behavior for broadband electromagnetic wave absorption, *Acta Materialia* **294**, 121154 (2025).
40. Liu, X. G. et al. Enhanced absorption bandwidth in carbon-coated supermalloy FeNiMo nanocapsules for a thin absorb thickness, *Journal of Alloys and Compounds* **506**, 826-830 (2010).
41. Tian, W. et al. Hybrid silica-carbon bilayers anchoring on FeSiAl surface with bifunctions of enhanced anti-corrosion and microwave absorption, *Carbon* **173**, 185-193 (2021).
42. Rozanov, K. N. Ultimate thickness to bandwidth ratio of radar absorbers, *IEEE Transactions on Antennas and Propagation* **48**, 1230-1234 (2000).

## Methods

### Sample preparation

The FeMnSiAl powdery absorbents were obtained by physical processing including arc melting, gas atomization, attritor milling and heat treatment. The doping mass fraction of Mn was denoted as $Fe_{85-x}Mn_xSi_{9.6}Al_{5.4}$ ($x$ = 0, 1.6, 3.2, 4.8, 6.4 wt.%).

The elemental Fe, Mn, Si, Al were proportionally mixed and then arc-melted in the Ar atmosphere (99.999%, 0.05 MPa). The melting state was maintained for 5 min with magnetic stirring. This procedure was repeated for 5 times to ensure the component uniformity in the obtained ingots. Subsequently, the $Fe_{85-x}Mn_xSiAl$ ingots were placed into a quartz atomization crucible, and then heated to a liquid state (~1450 $^oC$) through electromagnetic induction in the Ar atmosphere (99.999%, 1 MPa). The liquid steel was squeezed out from the bottom of the crucible by a pressure difference of 0.20 MPa, and immediately impacted into spherical particles by a simultaneous Ar flow of 8.00 MPa. Next, 10 g obtained $Fe_{85-x}Mn_xSiAl$ powders were added into an attritor milling jar with 800 g $ZrO_2$ balls (>95%, $\Phi$ 6 mm) and 70 g analytically pure ethanol, and then milled for 16 h at a rotation speed of 150 rpm. Finally, the flaky $Fe_{85-x}Mn_xSiAl$ powders were heated to the target temperature at a rate of 10 $^oC$/min in a vacuum (<0.1 MPa), held for 2 h, and then annealed by natural cooling.

The resultants were designated as FSA ($Fe_{85}Si_{9.6}Al_{5.4}$), $FM_{1.6}SA$ ($Fe_{83.4}Mn_{1.6}Si_{9.6}Al_{5.4}$), $FM_{3.2}SA$ ($Fe_{81.8}Mn_{3.2}Si_{9.6}Al_{5.4}$), $FM_{4.8}SA$ ($Fe_{80.2}Mn_{4.8}Si_{9.6}Al_{5.4}$), $FM_{6.4}SA$ ($Fe_{78.6}Mn_{6.4}Si_{9.6}Al_{5.4}$) based on the contents of Mn.

## Morphology and structure characterization

The micromorphology was observed by scanning electron microscopy (SEM, Hitachi S-4800). The elemental composition and mappings were investigated using inductively coupled plasma optical emission spectrometry (ICP-OES, Teledyne Leeman Labs Prodigy 7) and energy-dispersive spectroscopy (EDS, Oxford Ultim Max 40) attached to SEM.

The crystal structure and phase composition were characterized by the 2D wide-angle X-ray scattering (2D WAXS, TPS synchrotron, 15 keV, $\lambda$ = 0.826533 Å) and X-ray diffraction (XRD, Malvern Panalytical Empyrean 3.0 with Cu K$\alpha$1, $\lambda$ = 1.54060 Å, Bruker D8 Advance with Co K$\alpha$1, $\lambda$ = 1.78897 Å). Further micro-structural analysis and phase distribution were characterized by bright/dark field images, high-resolution (HR) probing of local structures, selected area electron diffraction (SAED) patterns and elemental distribution using transmission electron microscopy (TEM, FEI Tecnai F20). The specific atomic site occupation was analyzed by the Mössbauer spectrometer (Wissel ms500) and the extended X-ray absorption fine structure (EXAFS, SSRF BL17B) using the transmission mode.

## Rietveld refinement of XRD pattern

Rietveld refinement of the XRD data was performed using GSAS-II. For $FM_{3.2}SA$, the atomic coordinates were constrained according to SAED, XRD and EXAFS. Furthermore, the refined lattice parameters were guided by quantitative measurements from HR TEM. Grain size ($D$) and internal strain ($\varepsilon$) were also determined from XRD patterns, using the Scherrer method [43] and the Williamson-Hall method [44].

401 **Fits of EXAFS spectra**

402 Analysis and fitting of EXAFS spectra were performed with the Athena and Artemis programs of
403 the Demeter data analysis packages that utilize the FEFF6 program [45, 46]. The energy calibration was
404 conducted using Mn foil. A linear function was subtracted from the pre-edge region, then the edge
405 jump was normalized using Athena software. The $\chi$(k) data were isolated by subtracting a smooth,
406 third-order polynomial approximating the absorption background of an isolated atom. The $k^3$-
407 weighted $\chi$(k) data were Fourier transformed applying a Hanning window function ($\Delta k = 1.0$). For
408 EXAFS modeling, the global amplitude EXAFS (CN, R, $\sigma^2$ and $\Delta E$) were obtained by nonlinear
409 fitting, with least-squares refinement, of the EXAFS equation to the Fourier transformed data in R-
410 space, using Artemis software. EXAFS of the Mn foil was fitted and the obtained amplitude
411 reduction factor was set in the EXAFS analysis to determine the CNs in samples.

412

413 **Fits of Mössbauer spectra**

414 In the notation Fe(n), n denotes the number of nearest-neighbor Fe atoms. Fe(6), Fe(8) and Fe(4)
415 sextets were assigned to Fe substitution in the A2 phase, the body-centered site and the corner site
416 in the $D0_3$ supercell, respectively. To account for local structural disorder induced by dopant atoms,
417 an additional Fe(5) sextet was included [47, 48].

418 Since the magnetic moments in FeSiAl-based alloys arise predominantly from Fe-Fe exchange
419 interactions, the coordination number n strongly modulates the local magnetic moments at each Fe
420 site. This was directly manifested as variations in the hyperfine field ($H$). Initial $H$ of 31 T, 28 T, 24
421 T, 20 T yield robust fits to the experimental spectra across all four Fe environments [47-49].

422 Notably, XRD and EXAFS analyses reveal that Mn preferentially occupies the Fe(8) site. The

423 substitution perturbs the local magnetic environment of all Fe sites in the $D0_3$ phase, particularly
424 Fe(4). Under such conditions, introducing more discrete sextets with distinct *H* would obscure
425 physical interpretation without improving fidelity. Instead, a continuous distribution model for *H*
426 was adopted, enabling quantitative extraction of the averaged *H* while preserving mechanistic
427 clarity [50].
428
429 **First-principles calculations**
430 All first-principles calculations were performed based on density functional theory (DFT) using the
431 VASP (Vienna Ab initio Simulation Package) [51-53]. We constructed a 2×2×2 supercell based on the
432 bcc-Fe unit. The initial lattice parameters were set to the experimentally determined value (from
433 XRD, HRTEM and EXAFS).
434 The exchange-correlation energy of electrons was treated using the Perdew-Burke-Ernzerhof (PBE)
435 functional within the generalized gradient approximation (GGA). The cutoff energy of the plane-
436 wave was set to 400 eV. The Brillouin zone integration was performed using the Monkhorst-Pack
437 method, with a 6×6×6 k-point mesh. Self-consistent field (SCF) convergence was enforced to
438 $1.0\times10^{-6}$ eV per atom.
439 Structural relaxation was performed using the conjugate gradient algorithm, allowing full relaxation
440 of atomic positions until the Hellmann-Feynman force on any atom fell below 0.02 eV/Å.
441 Considering the ferromagnetism of bcc-Fe, all calculations included spin polarization. Magnetic
442 anisotropy energy (MAE) was computed based on the optimized structure, by incorporating spin-
443 orbit coupling (SOC) effect.
444

## Micromagnetic simulations

The micromagnetic simulations were carried out using Mumax3 software [54]. The calculations used a two-region model ($80 \times 80 \times 20$ nm$^3$) representing the $D0_3$-FeSiAl matrix and the $D0_3$-(Fe,Mn)SiAl region, with their local anisotropy directions distinguished according to the structural and first-principles analysis. Specifically, the easy axes of the $D0_3$-FeSiAl matrix were set as [100] and [001], with $M_s = 1.093 \times 10^6$ A/m and $K_1 = 1.610 \times 10^5$ J/m$^3$; the easy axis of the $D0_3$-(Fe,Mn)SiAl region was set as [010], with $M_s = 0.975 \times 10^6$ A/m and $K_1 = 0.836 \times 10^5$ J/m$^3$. The exchange stiffness coefficient was set as $1.359 \times 10^{-11}$ J/m.

The magnetization dynamics were governed by the Landau-Lifshitz-Gilbert (LLG) equation [55, 56],

$$\frac{\mathrm{d}\boldsymbol{M}}{\mathrm{d}t} = -\gamma \mu_0 (\boldsymbol{M} \times \boldsymbol{H}_{\mathrm{eff}}) + \frac{\alpha}{M_S} (\boldsymbol{M} \times \frac{\mathrm{d}\boldsymbol{M}}{\mathrm{d}t})$$

where $\boldsymbol{M}$ and $\boldsymbol{H}_{\mathrm{eff}}$ represent the magnetization vector and the effective anisotropy field vector, respectively, $\gamma$ is the gyromagnetic ratio, $\mu_0$ is the vacuum permeability, and $\alpha$ is the Gilbert damping coefficient. A SINC-pulse excitation was used for time-domain precession calculations. Phase maps were used to compare the response of the two magnetic regions at frequencies below and around the resonance. The supplementary simulations also include single-phase references.

## Magnetic characterization and field-swept FMR

The static magnetic structure and properties were determined by vibrating sample magnetometer (VSM, LakeShore 7400S), and directly observed by Lorentz transmission electron microscopy (LTEM, Thermo Spectra 200). The intrinsic variation in electromagnetic properties of distinct phases was observed by electrostatic force microscopy (EFM) and magnetic force microscopy (MFM), attached to atomic force microscopy (AFM, Jupiter XR).

Field-swept ferromagnetic resonance (FMR) spectra were recorded on the powder/silicone resin composites at 1 to 10 GHz for $FM_{3.2}SA$, and 2, 4, and 8 GHz for FSA reference. Forward and reverse field sweeps were used to assess sweep-direction-dependent shifts of spectral features. The two sweep directions were compared at the same frequency using a consistent characteristic field range. The dependence on sweeping direction is quantitatively assessed by the field difference between the two resonance centers, which is defined as the symmetric center between the peaks.

**Characterization of electromagnetic performance**

To characterize the electromagnetic performance, samples were prepared as coaxial rings with a thickness of ~2.0 mm, inner diameter of 3.0 mm and outer diameter of 7.0 mm. For composite comparisons, flaky powders were dispersed in wax at a mass ratio of 2:1 (3:1 for spherical powders) and pressed at ~10 MPa. For absorber coating, powders were dispersed in silicone resin, spray-coated onto the substrate and cured. The relative complex permittivity ($\varepsilon_r = \varepsilon' - j\varepsilon''$) and permeability ($\mu_r = \mu' - j\mu''$) were measured by impedance analyzer (E4991B Keysight, 1 MHz–1 GHz) and vector network analyzer (VNA, Agilent N5230, 0.1–10 GHz). The DC conductivity of the powder was measured using an ST2742 four-probe powder resistivity tester, under pressures increasing from 2.0 to 30 MPa.

**Joint fits of the dynamic effective anisotropy**

For field-swept FMR, each resonance was represented by derivatives of an absorptive Lorentzian and a dispersive Lorentzian, with adjustable mixing coefficients and a quadratic baseline. A single resonance component was used for 1–7 GHz. Two components were used for 8–10 GHz only where

the residual line shape required them.

The experimentally measured $\mu'$ and $\mu''$ were fitted simultaneously using the LLG/Polder description. The collective response was represented as [57, 58]

$$\chi_{\mathrm{col}}(\omega) = \mathrm{A}\,\frac{\omega_{\mathrm{M}}\left[\,\omega_{\mathrm{k}}(\omega) - i\,\alpha_{\mu}\,\omega\,\right]}{\left[\,\omega_{\mathrm{k}}(\omega) - i\,\alpha_{\mu}\,\omega\,\right]^2 - \omega^2}\ ,$$

with $\omega_{\mathrm{k}}(\omega) = \gamma\,\mu_0\,H_{\mathrm{k}}(\omega)$, $\omega_{\mathrm{M}} = \gamma\,\mu_0\,M_{\mathrm{S}}$. Here, $A$ accounts for amplitude, powder orientation and composite-volume factors. $\alpha_{\mu}$ is an effective relaxation coefficient.

In the constant-$H_{\mathrm{k}}$ model, $H_{\mathrm{k}}$ is frequency independent. Previous studies have derived the magnetic dispersion from natural resonance [56]:

$$\mu' = B + I_i\,\frac{1 - (f/f_{\mathrm{r}})^2\,(1-\alpha^2)}{\left[1 - (f/f_{\mathrm{r}})^2\,(1+\alpha^2)\right]^2 + 4\alpha^2\,(f/f_{\mathrm{r}})^2}\ ,$$

$$\mu'' = I_i\,\frac{\alpha\,(f/f_{\mathrm{r}})\left[1 + (f/f_{\mathrm{r}})^2\,(1+\alpha^2)\right]}{\left[1 - (f/f_{\mathrm{r}})^2\,(1+\alpha^2)\right]^2 + 4\alpha^2\,(f/f_{\mathrm{r}})^2}\ ,$$

where $f$ and $f_{\mathrm{r}}$ represent measurement and resonance frequency, respectively, $I_i$ represents amplitude factor, and $B$ is the background constant. Moreover, the fitting incorporated domain wall resonance, the corresponding complex magnetic permeability of which can be expressed as [56, 59]:

$$\mu' = 1 + \chi' = 1 + \chi_i\,\frac{1 - (\omega/\omega_{\mathrm{r}})^2}{\left[1 - (\omega/\omega_{\mathrm{r}})^2\right]^2 + (\beta\omega/\omega_{\mathrm{r}})^2}\ ,$$

$$\mu'' = \chi'' = \chi_i\,\frac{\beta\omega/\omega_{\mathrm{r}}}{\left[1 - (\omega/\omega_{\mathrm{r}})^2\right]^2 + (\beta\omega/\omega_{\mathrm{r}})^2}\ ,$$

where $\omega$ and $\omega_{\mathrm{r}}$ represent measurement and resonance angular frequency, respectively, $\chi_{\mathrm{i}}$ represents the initial magnetic susceptibility, and $\beta$ is the damping coefficient. The fitting of complex permeability employed a linear superposition model comprising three contributions: A2 and $D0_3$ natural resonance, and domain wall resonance. The natural resonance of dual $D0_3$ phases was fitted using a continuous model, with the initial resonance frequency set as 1.0 GHz. The relative weights of the A2 and $D0_3$ resonances are constrained by the fractions obtained from Rietveld refinement of

XRD data.

In the dynamic-$H_k$ model, the complex effective stiffness was described by [60]

$$H_k(f) = H'_k(f) - i\,H''_k(f) = H_{k,0} + \left(H_{k,\infty} - H_{k,0}\right)\frac{(-if/f_c)^{\beta}}{1+(-if/f_c)^{\beta}}\ ,$$

where $H_{k,0}$ is the low-frequency effective stiffness, $H_{k,\infty}$ is the high-frequency asymptote, $f_c$ is the characteristic frequency and $\beta$ is a fractional dispersion exponent. The real and imaginary parts of the measured permeability were optimized using one common parameter set, so that the same $H_k(f)$ must reproduce both magnetic dispersion and magnetic loss.

**Simulations of microwave absorption based on electromagnetic parameters**

The microwave absorption performance is evaluated in terms of reflection loss (*RL*) and radar cross section (RCS) reduction. *RL* can be calculated based on electromagnetic parameters [61]

$$RL = 20\lg\left|\frac{Z_{in}-Z_0}{Z_{in}+Z_0}\right|,\ \text{where}\ Z_{in} = Z_0\sqrt{\frac{\mu_r}{\varepsilon_r}}\tanh\left(i\left(\frac{2\pi fd}{c}\right)\sqrt{\mu_r\varepsilon_r}\right)\ .$$

where $Z_{in}$ and $Z_0$ represent the input impedance of the absorber and the characteristic wave impedance in free space (~377 Ω), respectively, $d$ is the thickness of the absorber, and $c$ is the speed of light in vacuum.

To overcome the limitations of evaluating performance only by thickness or absolute effective absorption bandwidth, and to objectively compare absorbers across different frequency bands, the relative absorption bandwidth ($W_{10}$) and dimensionless absorption efficiency ($E_{10}$) are introduced. $W_{10}$ is defined as

$$W_{10} = \frac{2\left(f_U - f_L\right)}{f_U + f_L}\ ,$$

where $f_U$ and $f_L$ are the upper and lower frequency bounds for $RL < -10$ dB, respectively. This metric eliminates the influence of center frequency, reflecting relative broadband performance.

$E_{10}$ is defined as

$$E_{10} = \frac{\triangle\lambda}{d} = \frac{c}{d}\left(\frac{1}{f_{\mathrm{L}}} - \frac{1}{f_{\mathrm{U}}}\right),$$

where $d$ is the thickness. It represents wavelength span covered per unit thickness, reflecting the wavelength-to-thickness compression efficiency. The $W_{10}$ - $E_{10}$ plots provide a framework to intuitively compare the comprehensive absorption advantages of materials across different frequency bands.

Moreover, we employed RCS simulation to model realistic microwave scattering. Compared with *RL*, RCS additionally incorporates extrinsic factors, such as the geometric shape of the target, wave characteristics, etc. RCS quantifies the power density of the electromagnetic wave scattered by a target, serving as a fundamental metric for assessing the detectability of an object [61]. A higher RCS corresponds to higher radar visibility. We used CST Studio Suite to conduct the simulation. The model consisted of a 1 m×1 m×2 mm copper plate and a 1 m×1 m coating with varied thickness. The coating material was defined as a homogeneous medium with frequency-dependent complex permittivity and permeability, which were obtained by experimental measurements. A plane wave was employed as the excitation source, with propagation direction normal to the plate surface. Open boundary conditions were applied in all directions to emulate free-space conditions. The simulation was performed at 1, 2 and 4 GHz. A far-field monitor was set up to record the backscattered field, and the monostatic RCS was extracted. The RCS reduction performance was evaluated by comparing the RCS values against that of the bare copper plate.

**Environmental stability measurements**

Anti-oxidation performance was evaluated using an integrated thermal gravimetric analyzer

(Netzsch STA449F3). Samples were heated from room temperature to 1000 °C, at a heating rate of 5 °C/min in air.

To evaluate the corrosion resistance of the samples, 10 mg of each sample was dispersed in 1 mL ethanol with 50 μL Nafion solution, and ultrasonically treated to form a homogeneous suspension. Electrochemical measurements were performed in a 3.5 wt.% NaCl aqueous solution using an electrochemical workstation (Chenhua CHI 760E). A standard three-electrode system was configured, containing a working electrode (50 μL suspension deposited on an ITO substrate), a counter electrode (1 cm × 1 cm Pt foil) and a reference electrode (saturated calomel electrode, SCE). The open-circuit potential (OCP) was recorded for 10 min.

The electrochemical impedance spectroscopy (EIS) was measured over a frequency range of $10^{-2} \sim 10^{6}$ Hz, with an AC amplitude of 10 mV. Nyquist and Bode spectra were jointly evaluated using a series solution resistance and two parallel resistor-constant-phase-element branches,

$$Z(\omega) = R_S + \frac{1}{\frac{1}{R_1} + Q_1 (i\omega)^{n_1}} + \frac{1}{\frac{1}{R_2} + Q_2 (i\omega)^{n_2}} ,$$

which is equivalent to $R_S$ - ( $R_1$ || $CPE_1$ ) - ( $R_2$ || $CPE_2$ ). For each constant-phase element, $Z_{CPE} = 1/Q(i\omega)^n$, where $Q$ is a pseudo-capacitance prefactor and $0 < n \leq 1$ describes non-ideal capacitive behaviour. The two branches capture distinguishable effective relaxation processes in the heterogeneous powder/Nafion/ITO electrode.

## References


43. Patterson, A. L. The Scherrer formula for X-Ray particle size determination, *Physical Review* **56**, 978-982 (1939).

44. Williamson, G. K. & Hall, W. H. X-ray line broadening from filed aluminium and wolfram, *Acta Metallurgica* **1**, 22-31 (1953).

45. Ravel, B. & Newville, M. ATHENA, ARTEMIS, HEPHAESTUS: Data analysis for X-ray absorption spectroscopy using IFEFFIT, *Journal of Synchrotron Radiation* **12**, 537-541 (2005).

46. Zabinsky, S. I. et al. Multiple-scattering calculations of x-ray-absorption spectra, *Physical Review B* **52**, 2995-3009 (1995).

47. Zhang, N. et al. The influence of annealing temperature on hyperfine magnetic field and saturation magnetization of Fe-Si-Al-Cr flake-shaped particles, *Journal of Alloys and Compounds* **672**, 176-181 (2016).

48. Han, M. & Deng, L. Understanding the enhanced microwave permeability of Fe-Si-Al particles by Mössbauer spectroscopy, *Journal of Magnetism and Magnetic Materials* **337-338**, 70-73 (2013).

49. Stearns, M. B. Internal magnetic fields, isomer shifts, and relative abundances of the various Fe sites in FeSi alloys, *Physical Review* **129**, 1136-1144 (1963).

50. Arzhnikov, A. K. et al. Hyperfine magnetic fields in partially disordered Fe-Si alloys with Si content near 25 at.%, *Physical Review B* **65**, 024419 (2001).

51. Kresse, G. & Furthmüller, J. Efficiency of ab-initio total energy calculations for metals and semiconductors using a plane-wave basis set, *Computational Materials Science* **6**, 15-50

(1996).

52. Kresse, G. & Joubert, D. From ultrasoft pseudopotentials to the projector augmented-wave method, *Physical Review B* **59**, 1758-1775 (1999).

53. Kresse, G. & Furthmüller, J. Efficient iterative schemes for ab initio total-energy calculations using a plane-wave basis set, *Physical Review B* **54**, 11169-11186 (1996).

54. Vansteenkiste, A. et al. The design and verification of MuMax3, *AIP Advances* **4**, 107133 (2014).

55. Saitoh, E., Miyajima, H., Yamaoka, T. & Tatara, G. Current-induced resonance and mass determination of a single magnetic domain wall, *Nature* **432**, 203-206 (2004).

56. Dillon, J. F. & Earl, H. E. Domain wall motion and ferrimagnetic resonance in a manganese ferrite, *Journal of Applied Physics* **30**, 202-213 (1959).

57. Gilbert, T. L. A Lagrangian formulation of the gyromagnetic equation of the magnetic field, *Physical Review* **100**, 1243 (1955).

58. Kittel, C. On the theory of ferromagnetic resonance absorption, *Physical Review* **73**, 155-161 (1948).

59. Wu, L. Z. et al. High frequency complex permeability of iron particles in a nonmagnetic matrix, *Journal of Applied Physics* **99**, 083905 (2006).

60. Fano, W. G., Boggi, S. & Razzitte, A. C. Causality study and numerical response of the magnetic permeability as a function of the frequency of ferrites using Kramers–Kronig relations, *Physica B: Condensed Matter* **403**, 526-530 (2008).

61. Wang, F., Li, W., Chen, Z. & Guan, J. Anticorrosive magnetic microwave absorbers by turbulent sol-gel method, *Journal of Materials Science & Technology* **230**, 205-218 (2025).

## Data availability

All data supporting the findings of this study are available in the Article and its Supplementary Information. The source data, the codes used for micromagnetic simulations, and additional data are available from the corresponding authors upon reasonable request.


## Acknowledgements

This research was supported by the National Natural Science Foundation of China (No. 52311530074), Key Research Project of Hubei province (No. 2024BAB113), the Fundamental Research Funds for the Central Universities (No. 104972026KFYjc0126) and the Innovation Team in Key Areas of the Innovation Talent Promotion Plan of MOST, China. The authors are grateful for the discussion with Prof. Dongsheng Xu.


## Author contributions

Y.X., Y.L., S.L. and Z.C. designed the experiments and carried out the materials preparation. Y.X. and N.X. conducted the microstructure characterization and analyzed the data. Y.X., C.L. and M.B. conducted the electromagnetic characterization and analyzed the data. Y.X., Y.K. and W.L. conducted the Lorentz TEM and MFM experiments, and analyzed the data. R.Z., Y.H. and Y.L. performed the first-principles calculations. J.G. supervised this project. Z.C., J.G. and Y.X. wrote and revised the paper with input from all authors. All authors discussed the results and commented on the paper.

## Competing interests

The authors declare no competing interests.

## Supplementary Files

This is a list of supplementary files associated with this preprint. Click to download.

- SupplementaryInformation.docx